

Journal of Materials Chemistry A

Accepted Manuscript



This is an *Accepted Manuscript*, which has been through the Royal Society of Chemistry peer review process and has been accepted for publication.

Accepted Manuscripts are published online shortly after acceptance, before technical editing, formatting and proof reading. Using this free service, authors can make their results available to the community, in citable form, before we publish the edited article. We will replace this *Accepted Manuscript* with the edited and formatted *Advance Article* as soon as it is available.

You can find more information about *Accepted Manuscripts* in the [Information for Authors](#).

Please note that technical editing may introduce minor changes to the text and/or graphics, which may alter content. The journal's standard [Terms & Conditions](#) and the [Ethical guidelines](#) still apply. In no event shall the Royal Society of Chemistry be held responsible for any errors or omissions in this *Accepted Manuscript* or any consequences arising from the use of any information it contains.

Cite this: DOI: 10.1039/c0xx00000x

www.rsc.org/xxxxxx

ARTICLE TYPE

Mesoporous Graphene-like Carbon Sheet: High-Power Supercapacitor and Outstanding Catalyst Support

Pengfei Zhang,^{*a} Zhen-An Qiao,^a Zhiyong Zhang,^a Shun Wan^a and Sheng Dai^{*a,b}

Received (in XXX, XXX) Xth XXXXXXXXX 20XX, Accepted Xth XXXXXXXXX 20XX

DOI: 10.1039/b000000x

Nowadays, continuous scientific endeavors are being directed toward low-cost, mild, scalable and reliable synthesis of graphene-based materials, in order to advance various graphene-related applications. So far, specific surface areas of current bulk graphene powders or graphene-like nanosheets are yet much lower than the theoretical value (2630 m²/g) of individual graphene, remaining a challenge for carbon chemists. Herein, mesoporous graphene-like carbon sheets with high specific surface area (up to 2607 m²/g) and high pore volume (up to 3.12 cm³/g) were synthesized by performing polyimide chemistry in the molten salt “solvent.” In this process, abundant pyromellitic dianhydride and aromatic diamine undergo polycondensation together with further carbonization in molten KCl-ZnCl₂, in which in-situ formed linear aromatic polyimide with a sp² hybridized carbon skeleton could be directly coupled and rearranged into two-dimensional graphene-like nanosheet around the “salt scaffold”. Carbon nanosheets with well-defined mesopores (~3.5 nm) could be easily obtained by washing salt melts in water, while those salts could be recovered and reused for subsequent reaction. The nitrogen atoms in amine also afforded the resulting carbon with uniform foreign atoms (nitrogen content = ~6%). Moreover, holey carbon sheets with well-dispersed and through-plane nanoholes (diameter: 5-10 nm) could be constructed by using different monomers. Being a potential electrode material in supercapacitor, the as-made carbon nanosheet possessed a significant specific capacitance (131.4-275.5 F g⁻¹) even at a scan rate of 2000 mV s⁻¹. Additionally, powerful nanohybrids of carbon sheet-Co₃O₄ were also prepared with good performance in the aerobic oxidation of alcohols and amines to aldehydes and imines, respectively.

1. Introduction

Because of their high theoretical specific surface area (SSA, 2630 m²/g), high intrinsic electrical conductivity, high chemical stability, and controllable elemental composition, graphene or graphene-like nanosheets are currently of high scientific and technological interest in a variety of fields, and more and more efforts are being devoted to the development of simple routes to this target materials.¹⁻⁶ Though various synthetic methods, such as epitaxial growth, chemical vapor deposition, substrate-free gas phase synthesis and total organic synthesis, *etc.*, have been established, the industrial production of bulk graphene powder still relies on the chemical exfoliation of graphite minerals.⁷⁻¹⁰ Recently, Antonietti and co-workers introduced an interesting approach converting glucose to graphene or graphene-like nanoplatelets through graphitic carbon nitride-templated or activation processes, which can partly overcome some problems in this topic.¹¹⁻¹⁴ To date, the SSA values of real bulk graphene or graphene-like nanosheet derived from state-of-the-art methods remain far from the theoretical value (2630 m²/g), mainly due to the overlap and stacking of the individual layers.¹⁵ Besides developed SSA, pore structure is another key issue controlling the accessibility of graphene-like nanosheets. Actually, porosities of

existing graphene-like nanosheets were mainly dominated by micropores, in term of N₂ sorption measurements.¹⁵⁻¹⁶ To this end, the construction of carbon nanosheets with mesoporous domain is highly welcomed and should significantly benefit carbon-based applications, such as supercapacitor and heterogeneous catalysis, because, in above-mentioned processes, the narrow pores often cause the transport of ions or diffusion/mass transfer to be the rate-controlling factor limiting their efficiency in large degree.¹⁶⁻²⁰ For example, in the carbon-based electrical double layer capacitor, achieving fast energy delivery at high charge/discharge rate urgently requires such mesoporous carbon nanosheet, since the broad pore channel and open surface are fully accessible to electrolyte/ion adsorption and transport, even those large ions in organic electrolytes.²¹⁻²⁴ In this contribution, we show the direct fabrication of graphene-like nanosheet with a SSA value of 2607 m²/g and well defined mesopores (~3.5 nm) by a versatile ionothermal condensation of abundant aromatic diamines and pyromellitic dianhydride (PMDA), namely, by performing the polyimide chemistry in molten salts. The essence of our strategy is directly condensing and rearranging one-dimensional (1D) aromatic polymer with a sp² hybridized carbon skeleton to two-dimensional (2D) graphene-like nanosheet in the presence of chemically inert “molten salt scaffolds”. The deep eutectic salt

mixture with low melting point (near 200 °C) and high decomposition temperature (over 1000 °C) can provide a wide temperature range for keeping the polymerization and activation in liquid environment.²⁵ If good miscibility of the carbonizing polymer in the “salt solvent” is retained over a main part of the reaction pathway, the formed nanosheet intermediates should be fully surrounded by salt clusters starting at the initial stage. Therefore, relatively thin carbon nanosheets could be expected after the salt phase is removed by simple washing in water.

More recently, introducing nitrogen functionality into sp² carbon structure was found to effectively modify the electronic structure, the Fermi level as well as surface basic/coordinating property of the pristine carbon, and the resulting nitrogen-doped carbon afforded remarkable performance in various applications, such as solid support for catalysis.²⁶⁻²⁸ Wang and co-workers recently illustrated that Pd catalysts supported on nitrogen-doped carbons showed superior activity in the aerobic oxidation of hydrocarbons and alcohols.²⁹ In the robust aromatic polyimide, the sp² nitrogen atoms trapped in sp² carbon frames seem to be an ideal and natural choice for fabricating nitrogen-doped carbons. The graphene-like nanosheets by our method were also shown to be modified by considerable nitrogen elements. Further electrochemical and catalytic tests illustrated their excellent activity and stability in high-power supercapacitors and aerobic oxidations.

2. Experimental Section

2.1 Chemicals

Chemicals involved in the material synthesis and catalytic tests in this work include benzidine (≥98%), *p*-phenylenediamine (≥97%), 3,3'-diaminobenzidine (99%), pyromellitic dianhydride (97%), anhydrous ZnCl₂ (99.99%), KCl (≥99%), Co(NO₃)₂·6H₂O (≥98%), benzyl alcohol (99.8%), cyclohexanol (≥99%), benzylamine (≥99%). All the above chemicals were purchased from Sigma-Aldrich Chemicals in the US and used without further treatment. The (±)-1-phenylethyl alcohol (>98%) was received from TCI Chemicals in USA.

2.2 Synthesis of Carbon Nanosheets

In a typical process for MCS-1, 1 mmol pyromellitic dianhydride, 1 mmol benzidine and metal chlorides salts (KCl/ZnCl₂ = 51/49 by molar) in the weight ratio of reactants/solvent = 1:9 (solvent: KCl/ZnCl₂), were mixed and homogenized with a ball mill (~5 minutes). Unless otherwise mentioned, this ratio of 1:9 was used throughout this study. The homogeneous mixture was filled into an Al₂O₃ crucible and then transferred to the tube furnace within N₂ atmosphere (200 mL/min). The furnace was ramped to reaction temperature (325–1000°C) at 3.33°C/min and there dwelled for 1 h to allow complete conversion. After natural cooling to ambient temperature, the resulting products were crushed into powders and thoroughly washed with water and 3M HCl solution in order to dissolve the salts. The product was then collected from the dispersion by filtration. The wet carbon samples were finally dried in vacuum at 80°C for 24 h.

For the synthesis of MCS-2 and MCS-3, different amines were used in place of benzidine under the same reaction conditions. For the preparation of MCS-1@180, 1 mmol pyromellitic dianhydride and 1 mmol benzidine were dissolved in ionic liquids

(BmimCl: 1 g; BmimTf₂N: 4 g). The mixture in an open glass reactor was heated to 100°C for 5 h under stirring and then heated to 180°C for another 2 h. The final product was thoroughly washed with H₂O and ethanol and then dried in vacuum at 80°C for 24 h.

2.3 Synthesis of Co₃O₄@MCS-1

The Co₃O₄@MCS-1 hybrid material was prepared by the wetness impregnation method: 250 mg of Co(NO₃)₂·6H₂O was first dissolved in 1 mL of deionized water and then 250 mg of MCS-1@800 material was added into this solution. The resulting slurry was dried in an air oven at 110°C overnight and then thermally heated in N₂ at 350°C for 2 h in a tube furnace (heating rate: 5°C/min).

2.4 Salt recycling test

When the first run finished, the resulting mixture was thoroughly washed in 200 mL deionized water and then the liquid layer was collected by filtration. The resulting solution was then concentrated under reduced pressure at 80°C. The white solid was obtained and dried in a vacuum oven at 100°C for 24 h. Finally, the recovered salts were used in the subsequent reaction.

2.5 Typical procedure for aerobic oxidation of alcohols and amines

In a typical oxidation, 0.5 mmol substrate, 0.5 mmol methoxybenzene (internal standard), 5 mL *o*-xylene and 20 mg Co₃O₄@MCS were added into a 10 mL three-neck glass-reactor, which was fitted with a magnetic stirrer, a reflux condenser (1°C) and an O₂ inlet tube. The reaction was performed at 130°C in an oil bath with magnetic stirring (stirring rate: 1000 rpm). A stream of molecular oxygen was conducted into the reaction mixture and controlled by a flowmeter at a constant flow rate (5 mL min⁻¹). After completion of the reaction, the reaction mixture was weighed, and the liquid phase of the reaction mixture was collected by filtration for GC and GC-MS analysis.

2.6 Electrochemical Experiments

For the electrochemical experiments, 5.0 mg of the as-prepared material, 1.0 mg of onion-like carbon, and 7.5 μl 5 wt% Nafion solution were first mixed in 1.0 ml of isopropanol, and was dropcasted on a well-polished glassy carbon electrode to yield a loading of ~ 500 μg cm⁻². Cyclic voltammeteries (CVs) were carried out in 1.0 M Na₂SO₄ from -1.0 to 0 V vs. SCE at different scan rate. The specific capacitance (C_g) was calculated from the CV curve following the formula:

$$C_{sp} = \frac{\int i(E)dE}{2\Delta E m \nu}$$

where C_{sp} is the specific capacitance of individual sample. *i*(*E*) is the instantaneous current, $\int i(E)dE$ the total voltammetric charge obtained by integration of positive and negative polarizations in a cyclic voltammogram, Δ*E* is the potential window width, *m* is the mass of the sample in the electrode, and *v* is the scan rate.

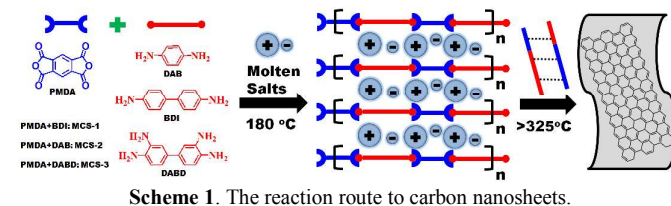
2.7 Characterization

For SEM and TEM characterization, samples were dispersed in ethanol using an ultrasonic bath. The final suspensions were

transferred to lacy carbon-coated 200-mesh copper TEM grids and dried in ambient air prior to electron microscopy analysis. Specimens were then characterized using a Hitachi HD-2000 operating in STEM mode using a secondary electron (SE) and/or bright-field STEM detector operating at 200 kV. Nitrogen adsorption isotherms were measured at -196°C using a TriStar 3000 volumetric adsorption analyzer manufactured by Micromeritics Instrument Corp. (Norcross, GA). Before adsorption measurements, the samples were degassed in flowing nitrogen at 150°C overnight. The specific surface area of the samples was calculated using the Brunauer-Emmett-Teller (BET) method within the relative pressure range of 0.05 to 0.20. Pore size distributions were calculated using the BJH model. The total pore volume was determined from the amount of N_2 uptake at a relative pressure of $P/P_0 = \sim 0.95$. X-ray diffraction patterns were recorded on a Siemens D5005 diffractionmeter with Ni-filtered $\text{Cu K}\alpha$ radiation operating at 40 kV and 40 mA.

3. Results and Discussion

3.1 Synthesis and characterization of graphene-like nanosheets



Initially, the condensation between PMDA and benzidine (BDI) was studied, and the deep eutectic salt mixture KCl/ZnCl_2 (molar ratio: 51/49) with a melting point of 230°C was selected as the solvent for polymerization and subsequent activation ($325\text{--}1000^{\circ}\text{C}$) (Scheme 1). In order to totally dissolve those organic precursors, the weight ratio of polymer precursors/molten salts was kept at 1/9 unless other states. Controlled synthesis for the corresponding polyimide at 180°C was carried out in ionic liquid (1-butyl-3-methylimidazolium chloride: $[\text{Bmim}]\text{Cl}$) or organic solvent (*m*-cresol). After carbonization under nitrogen atmosphere at desired temperature and aqueous removal of the salt porogen were performed, highly porous carbons were got, appearing as voluminous black powders. Those as-made materials were labeled by MCS-1@ 325 , etc., in which the last number represented the carbonization temperature (Scheme 1).

Thermal gravimetric analysis of reaction precursors showed that negligible carbon residue was obtained via the direct carbonization of PMDA or BDI, whereas a significant carbonization yield (15%) was observed with the physical mixture of PMDA and BDI, revealing that the temperature for forming stable polyimide structure is lower than the boiling points of two monomers and confirming the possibility of using this kind precursor to generate carbons (Figure 1a). As has been discussed in numerous reports, below 200°C , the condensation of amine- and anhydride-bearing monomers progresses effectively only via water elimination.³⁰ This is corroborated by the vanishing of N-H vibrational modes of BDI in Fourier transform infrared spectroscopy for as-made samples (Figure 1b), while at the same time these peaks from characteristic function groups in

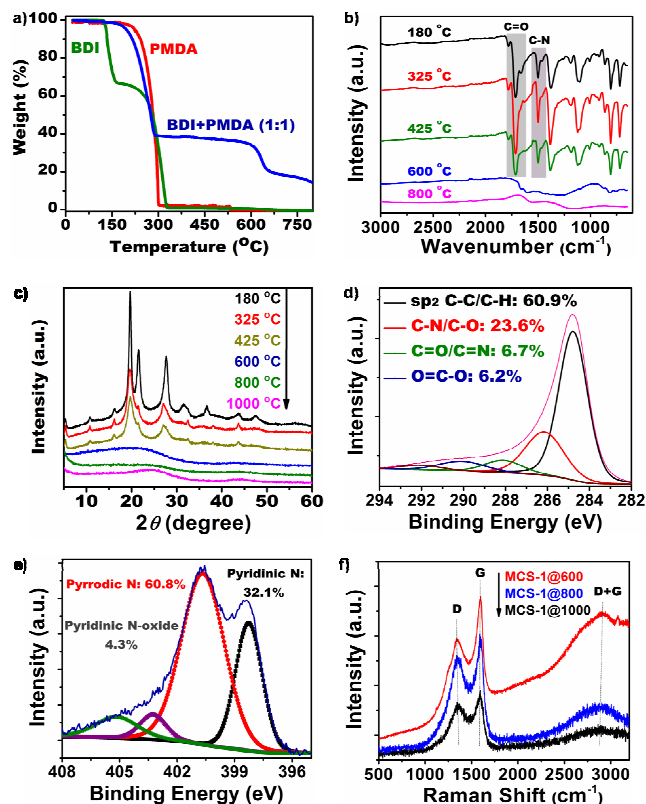


Figure 1. a) Thermal gravimetric analysis plots of carbon precursors in N_2 ; BDI: benzidine, PMDA: pyromellitic dianhydride; b) Fourier transform infrared spectroscopy of MCS-1 samples from different temperatures; c) X-ray powder diffraction patterns of MCS-1 samples from different reaction temperatures; d) and e) X-ray photoemission spectroscopy of MCS-1@800 sample (C1s and N1s); f) Raman spectra of MCS-1 samples from different temperatures.

polyimides gradually diminished in intensity and then disappeared in samples obtained at higher temperatures ($\geq 600^{\circ}\text{C}$). Upon heating to higher temperatures, the 1D polyimide chain might undergo organic group decomposition and structural rearrangement toward a stable network. X-ray powder diffraction analysis further confirmed this conclusion because, under increasing reaction temperature, the crystalline polyimides with sharp reflection peaks gradually transferred to graphitic carbons with broad (002) and (110) humps (Figure 1c). High resolution C 1s X-ray photoelectron spectroscopy (XPS) analysis of MCS-1@800 sample revealed that the carbon nanosheet was primarily made up of sp^2 type C-C/C-H bonds (60.9%) (Figure 1d). Promisingly, the nitrogen rich amine monomer resulted in the carbon nanosheet with a remarkable nitrogen content of 5.9% (Atomic %, XPS surface analysis), and those nitrogen elements were evenly dispersed on the carbon nanosheet, as seen in the elemental mapping picture (Figure S1). Further N 1s envelope analysis indicated a high pyrrolic surface character (400.6 eV; 60.8 %) and contributions from pyridinic motifs (398.3 eV; 32.1 %) (Figure 1e). In addition, it must be underlined that the molten salt “solvent” could promote the polycondensation process and significantly contribute to the carbonization yield; for instance, the MCS-1@800 material can achieve an acceptable yield (38%), much higher than that attained by only thermal treatment (15%, from TGA data).

Scanning electron microscopy (SEM) images depict the

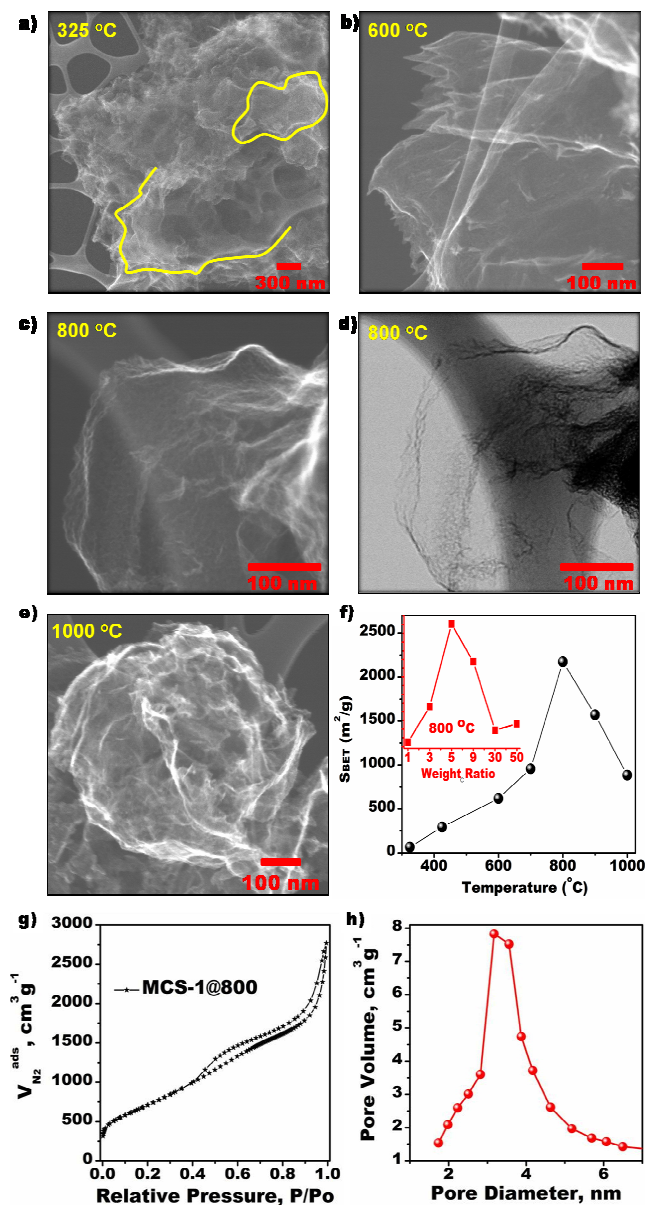


Figure 2. a)-e) SEM and TEM images of MCS-1 samples from different temperature; f) The relationship between reaction temperature and BET specific surface area for MCS-1 samples. The inset shows the effect of salt amount (weight ratio = salts/carbon precursors) on BET specific surface area; g) N_2 sorption isotherm of MCS-1@800 sample (salts/carbon precursors = 5/1 by weight) at 77 K and h) the corresponding pore size distribution.

overall evolution of morphologies from samples under increasing reaction temperature (Figure 2). Note that the local sheet-like structure appears at a temperature of as low as 325°C, suggesting that under current ionothermal conditions, these sp^2 C-X bonds (X = C, O or N) in polyimide might be easy to perform macroscopical cross-coupling and rearrangement toward large fragments of layers (Figure 2a). It can be seen from the SEM image that the product becomes dominated by the sheet structure starting at 600°C (Figure 2b, Figure S2). High-resolution SEM and transmission electron microscopy (TEM) images of MCS-1@800 show a local graphene-like structure with a crumpled sheet (Figure 2c, 2d). The morphology of the carbon sheet becomes much frizzier upon higher activation temperature (e.g.

1000°C, Figure 2e). The disordered nanosheets were also confirmed with Raman spectroscopy, which contained a D band at 1345 cm^{-1} , a G band at 1590 cm^{-1} and a D+G band at 2919 cm^{-1} (Figure 1f). The D band around 1350 cm^{-1} arises from disorder, but it is relatively weak compared to the G band representing sp^2 bonded graphitic carbons.

Table 1. Summary of BET surface areas and pore volumes for carbon sheets.^a

Sample	S_{BET} (m^2/g)	Pore Volume (m^3/g)
MCS-1@180	113	0.14
MCS-1@325	67	0.12
MCS-1@425	293	0.39
MCS-1@600	619	0.53
MCS-1@700	956	0.74
MCS-1@800	1249	0.83
MCS-1@800	1659	1.23
MCS-1@800	2607	3.12
MCS-1@800	2174	1.58
MCS-1@800	1386	1.07
MCS-1@800	1461	1.07
MCS-1@900	1572	1.45
MCS-1@1000	882	0.73
MCS-2@800	999	1.20
MCS-3@800	2104	1.15

^a Weight ratio of carbon precursors to molten salts.

Regarding N_2 sorption behavior for the carbon sheet system, a strong increase of the SSA along with thermal treatment temperature was observed, while MCS-1@900 broken this trend, as its SSA value of 1572 m^2/g was decreased compared to values for MCS-1@800 (Figure 2f, Table 1). It seems like that 800 °C is a suitable temperature for the accessible surface and overall porosity, and higher reaction temperature may lead to partial structure collapse. The carbonization processes at 800 °C with different monomer concentrations were then performed and it turned out to be highly crucial for the porosity control. We assume that a precise ratio of carbon source to molten salt is necessary for two possible reasons: a) There is a minimum amount of molten salts for completely dissolving monomers and intermediates, avoiding premature phase separation; b) On the contrary, excessive salts would make this polymerization in an extremely low concentration, which would influence the formation of continuous carbon networks. The optimized condition here was carbon precursor/molten salt = 1/5 by weight, while both lower and higher monomer concentrations would lower the SSA values. The resulting carbon nanosheet MCS-1@800 presented a Type IV/H₃ reversible N_2 sorption isotherm (77 K) presumed to be related to huge outer surface features and the presence of irregularly mesoporous domains (Figure 2g). The BET SSA of MCS-1@800 could reach 2607 m^2/g , significantly higher than previously reported values for bulk graphene or graphene-like nanosheets, and this value is exceptionally close to the theoretical SSA of single-layer graphene (2630 m^2/g).¹⁰⁻¹⁵ In particular, the pore size distribution analysis indicated that MCS-1@800 was actually dominated by mesopores (pore size: ~3.5 nm) and that its total pore volume is ultrahigh (3.12 cm^3/g at $P/P_0 = \sim 0.95$), providing a vast domain for mass transfer and exposing reactive sites (Figure 2h). We interpret the formation of a mesostructure with high SSA to be a consequence of irregularly combining three-dimensional carbon scaffolds and graphene-like fragments, in which those regions between corrugated sheets are

responsible for mesopores and the extremely thin platelet structure is the key point for high SSA. The formation of such nanostructure seems to be related to the promotion from ZnCl_2 salt. Controlled synthesis by carbonization of PMDA and BDI in molten LiCl/KCl at 425°C resulted in a carbon sample with lower SSA ($87\text{ m}^2/\text{g}$), and no product was obtained when the process was performed at 800°C or higher temperature (Table S1). The sharp contrast between LiCl/ZnCl_2 and LiCl/KCl reveals that the Lewis acid ZnCl_2 melt, which might coordinate with the nitrogen sites on the polyimide, is catalyzing the formation of layer structure, in some degree.

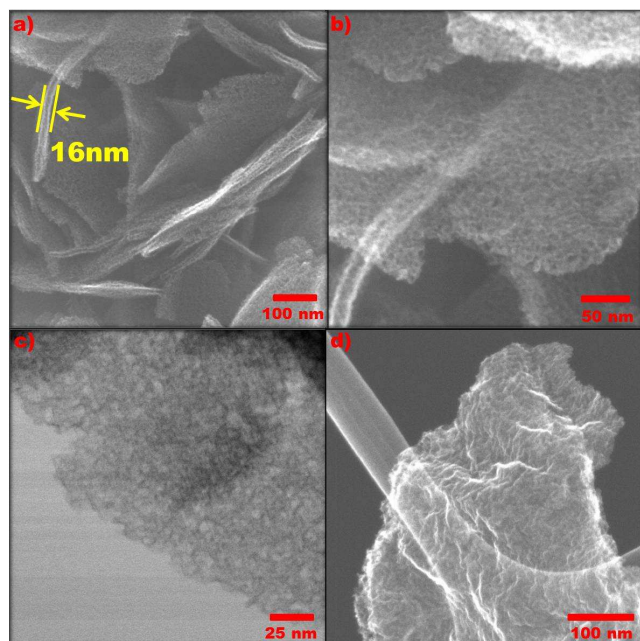


Figure 3. a) and b) SEM images of MCS-2@800; c) TEM image of MCS-2@800; d) SEM image of MCS-3@800.

In an endeavor to expand the scope of this method, similar polycondensations with 1,4-diaminobenzene (DAB) or 3,3'-diaminobenzidine (DABD) as amino monomers were carried out under optimized conditions, resulting in porous nanosheets with unique morphologies (labeled by MCS-2@800 and MCS-3@800, respectively; Scheme 1). The SEM images of MCS-2@800 clearly show stacked clusters of carbon nanoplates (Figure 3a, Figure S3). It should be emphasized that these carbon plates are much thicker ($\sim 16\text{ nm}$) than common graphene-like sheets, and surprisingly hold well-dispersed nanoholes throughout the plate (Figure 3b, 3c). In principle, these nanoholes with 5-10 nm diameters can nicely overcome the barrier problem of lamellar materials in mass transfer. Though the holey structure increases the number of active edges to some degree, the SSA of MCS-2@800 ($999\text{ m}^2/\text{g}$) is still lower than that of MCS-1@800. It is acceptable, since the enhanced plate thickness and pore size would largely decrease the SSA. When another monomer-DABD was used, a carbon nanosheet was obtained with a more wrinkled surface (MCS-3@800), as shown in the SEM and TEM images (Figure 3d, Figure S4). Moreover, MCS-3@800 is highly porous with an SSA of $2104\text{ m}^2/\text{g}$.

One of the general problems in the fabrication of porous materials is the difficulty of recovering and reusing the porogen/template. In the current strategy, the salt porogen could

simply be recycled by washing the products with water, and then concentrated under reduced pressure. In this effort, the synthesis of MCS-1@800 was investigated as an example. We found that the recovery ratio of salts was satisfactory ($\sim 95\text{ wt}\%$) and the structure-directing activity of the recovered salts was fully retained in the subsequent cycle. The final product possessed a curled paper-like morphology (Figure S5) with high SSA ($2477\text{ m}^2/\text{g}$). Therefore, one can imagine a simple closed-loop process including salt recycling that could result in the required high-SSA carbon sheets.

2.2 Supercapacitor Study

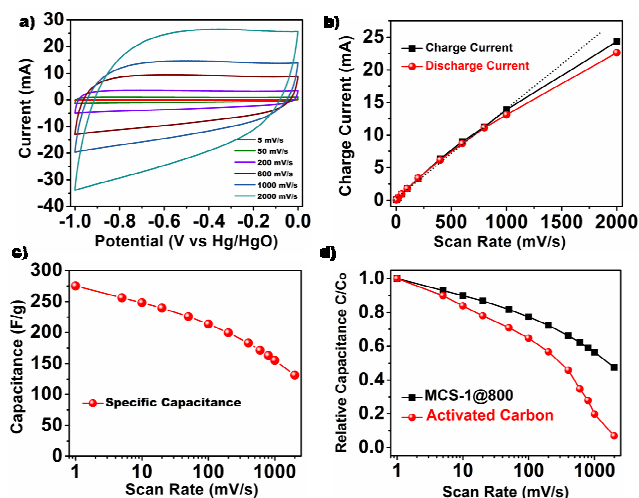
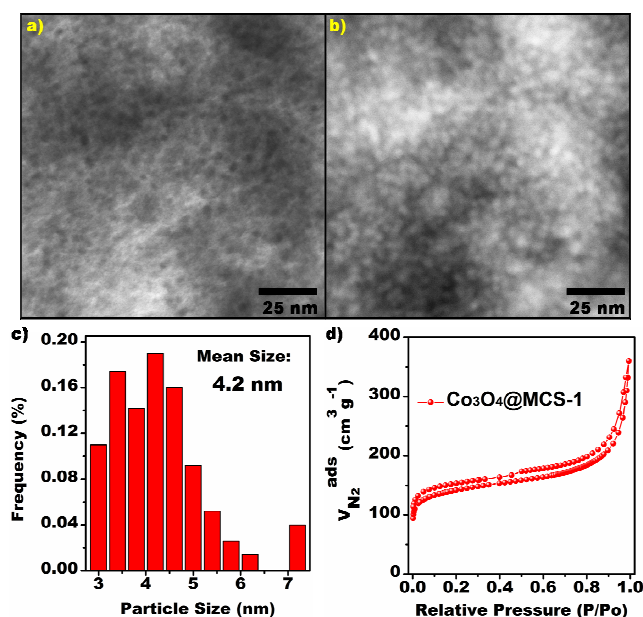


Figure 4. a) Cyclic voltammograms of MCS-1@800 sample recorded at 50 scan rates from 5 mV/s to 2000 mV/s ; b) Evolution of the charge/discharge current versus scan rate; c) Evolution of the specific capacitance versus scan rate; d) Evolution of the relative capacitance versus scan rate for graphene-like sheet and activated carbon.

The above characterization results clearly demonstrate the unique features of as-made carbons, such as the abundant sheet structure, a mesostructure with both high SSA and high pore volume, and uniform nitrogen doping, arguing for its promising potential as electrode material or catalyst support. Firstly, the mesoporous MCS-1@800 sample ($S_{\text{BET}} = 2607\text{ m}^2/\text{g}$) was used as the electrode for the supercapacitor in a three-electrode system. The cyclic voltammetry (CV) curve for MCS-1@800 sample in a basic (6 M KOH) media showed a nearly rectangular shape between -1 V and 0 V , suggesting the double-layer capacitance behavior (Figure 4a). It should be noteworthy that the rectangular shape was well retained even at a high scan rate (2000 mV s^{-1}) and this result illuminates the unrestricted motion of electrolyte in the pores at the slow double-layer formation situation.³¹⁻³² A linear dependence of the charge/discharge current on the scan rate was obtained up to at least 1000 mV s^{-1} in the capacitive region, indicating a high power ability for the electrode (Figure 4b). Control CVs for activated carbon (From Bulk Reef Supply) could only maintain the rectangular shape up to 600 mV s^{-1} , while curves from higher scan rates ($800\text{--}2000\text{ mV s}^{-1}$) showed an elliptical shape, in agree with previous observation (Figure S6).³³ For example, the activated carbon from waste tea with a high SSA of $2841\text{ m}^2/\text{g}$ can only retain the rectangular shape at voltage sweep rates less than 100 mV s^{-1} .³³ The specific capacitance was then calculated based on the integrated area of

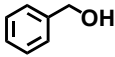
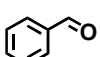
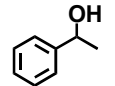
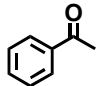
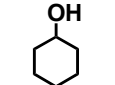
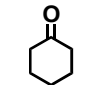
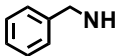
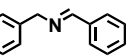


CVs, and the correlation between the specific capacitance and the **Figure 5.** a) and b) Bright- and dark-field TEM images of $\text{Co}_3\text{O}_4@\text{MCS-1}$ sample; c) Co_3O_4 particle size distribution; d) N_2 sorption isotherm of $\text{Co}_3\text{O}_4@\text{MCS-1}$ sample at 77 K.

scan rate is presented in **Figure 4c**. The $\text{MCS-1}@800$ sample holds a specific capacitance of 275.5 F g^{-1} at 1 mV s^{-1} . Notably, a relatively good capacitance of 131.4 F g^{-1} was observed even at a scan rate of 2000 mV s^{-1} . **Figure 4d** showed a comparison between $\text{MCS-1}@800$ sample and activated carbon for relative capacitances at different scan rates. The relative capacitance of activated carbon fell quickly at a higher scan rate, revealing a severe decrease in the instantaneous power of activated carbon relative to mesoporous carbon nanosheet because of the limitation of ion transfer in the inner microporous network of the activated carbon. These results distinctly highlight the excellent electrochemical performance of as-made carbon nanosheets.

2.3 $\text{Co}_3\text{O}_4@$ Carbon Hybrid Materials for Aerobic Oxidations

Table 2. Catalytic results of $\text{Co}_3\text{O}_4@\text{MCS-1}$ in the aerobic oxidation of alcohol and amine.^a

Entry	Substrate	Product	Catalyst	T (°C)	t (h)	Conv. (%)	Sel. (%)
1			-	130	16	2	-
2			$\text{MCS-1}@800$	130	16	2	-
3			$\text{Co}_3\text{O}_4@\text{MCS-1}$	130	16	95	98
4 ^b			Co_3O_4 NP	130	16	10	91
5			$\text{Co}_3\text{O}_4@\text{AC}$	130	16	35	91
6 ^c			$\text{Co}_3\text{O}_4@\text{MCS-1}$	130	16	98	95
7 ^d			$\text{Co}_3\text{O}_4@\text{MCS-1}$	130	16	100	95
8 ^e			$\text{Co}_3\text{O}_4@\text{MCS-1}$	130	16	100	96
9				130	16	93	97
10			$\text{Co}_3\text{O}_4@\text{MCS-1}$	145	24	67	95
11			$\text{Co}_3\text{O}_4@\text{MCS-1}$	60	16	100	94

a) Reaction condition: Substrate 0.5 mmol, Catalyst 20 mg, o-xylene 5 mL, O_2 1 atm; the reaction was monitored by GC. b) Co_3O_4 nanoparticle 4 mg. c) Second cycle to test the reusability of the catalyst. d) Third cycle to test the reusability of the catalyst. e) Fourth cycle to test the reusability of the catalyst.

In the subsequent work, we tried to use the $\text{MCS-1}@800$ sample to support an inexpensive and highly available cobalt species for aerobic oxidation. The solid catalyst with Co_3O_4 nanoparticles supported on $\text{MCS-1}@800$ was prepared by a facile and scalable wetness impregnation method.³⁴ It was denoted as $\text{Co}_3\text{O}_4@\text{MCS-1}$. TEM images of $\text{Co}_3\text{O}_4@\text{MCS-1}$ show that small metallic nanoparticles are evenly embedded in a carbon matrix (**Figure 5a, 5b**). Detailed analysis of the particle-size distribution confirmed that the mean size of these particles is 4.2 nm, smaller than Co_3O_4 nanocrystals on graphene recently synthesized (**Figure 5c**).^{6, 35, 36} The phase giving rise to the formation of Co_3O_4 was then confirmed by x-ray diffraction (**Figure S7**). The final Co_3O_4 content in the $\text{Co}_3\text{O}_4@\text{MCS-1}$ was determined to be 19% by thermal gravimetric analysis of this hybrid material in air (**Figure S8**). After incorporating such amount of Co_3O_4 nanoparticles into the carbon nanosheet, the porous structure was still retained, and the hybrid catalyst possessed a SSA value of $490 \text{ m}^2/\text{g}$ (**Figure 5d**).

To investigate the performance of the $\text{Co}_3\text{O}_4@\text{MCS-1}$ catalyst in aerobic oxidation, selective liquid-phase oxidation of benzyl alcohol with molecular oxygen (1 atm) was initially selected as a model process. Only a small amount of benzyl alcohol (2%) can be transformed in the blank test at 130°C , and the $\text{MCS-1}@800$ support alone did not show any catalytic activity (**Entries 1-2, Table 2**). Catalyzed by $\text{Co}_3\text{O}_4@\text{MCS-1}$, the oxidation afforded a 95% benzyl alcohol conversion with benzaldehyde as the main product (**Entry 3, Table 2**). Controlled oxidation by Co_3O_4 nanoparticles under the same reaction condition led to a 10% benzyl alcohol conversion, while a moderate conversion (35%) was obtained by $\text{Co}_3\text{O}_4@\text{Activated Carbon}$ (**Entries 4-5, Table 2**). Based on these catalytic results above, $\text{Co}_3\text{O}_4@\text{MCS-1}$ could be considered as an efficient catalyst in the aerobic oxidation of benzyl alcohol, and the introduction of this mesoporous carbon nanosheet support should be the origin of enhancement. Being a solid catalyst, $\text{Co}_3\text{O}_4@\text{MCS-1}$ can be easily recovered by centrifugation and reused at least three times without any loss of efficiency (**Entries 6-8, Table 2**). The liquid phase of the reaction mixture was collected by hot filtration after the reaction and analyzed by inductively coupled plasma mass spectrometry.

A very low amount of dissolved cobalt ($\sim 0.2\%$ of the total cobalt) was detected in the solution, indicating that the $\text{Co}_3\text{O}_4@\text{MCS-1}$ catalyst indeed functioned in a heterogeneous manner.

To illustrate the general applicability of the $\text{Co}_3\text{O}_4@\text{MCS-1}$ catalyst, aerobic oxidations of other alcohols and amines were then studied. The Co_3O_4 -catalysed oxidation of 1-phenylethanol proceeded very selectively to give acetophenone as a product (**Entry 9, Table 2**). This novel catalyst also worked well in the selective oxidation of cyclohexanol to cyclohexanone, but under a higher reaction temperature (**Entry 10, Table 2**). Moreover, the oxidative coupling of benzylamine to *N*-benzylidene benzylamine could be completed by this $\text{Co}_3\text{O}_4@\text{MCS-1}$ catalyst

under mild conditions: at a low temperature (60°C) and a low laboratory pressure of O₂ (1 atm) (Entry 11, Table 2).

3. Conclusion

In summary, it was shown that it is possible to create well-defined mesoporous graphene-like carbon nanosheets with both high surface area and high pore volume. The key point of this efficient synthesis is carrying out the dianhydride + diamine reaction within a “molten-salt clusters” atmosphere, a synergistic combination of polymerization, cross-coupling, and rearrangement in one system, which gives opportunities for direct transformation of in situ-produced 1D polyimide chains with sp² carbon units into hierarchical nanosheets scaffolded by molten salt. The high porosities rely on the featured morphology that couples very thin carbon fragments by 3D carbon networks. The most important advantage of the resulting carbon decidedly comes from the mesoporous sheet structure with high SSA (pore size: 3.5 nm, S_{BET} = 2607 m²/g, pore volume: 3.12 cm³/g). Unlike microporous materials such as activated carbons, zeolites, covalent-organic frameworks, or metal-organic frameworks, mesoporous graphene-like systems with extremely high SSA can afford much more accessible sites for catalysis and at the same time largely accelerate ion/mass transport and diffusion. As expected, the carbon nanosheet as a promising electrode for supercapacitors showed high capacity and excellent rate capability. In another important field-heterogeneous catalysis, the carbon nanosheet–Co₃O₄ hybrid material was found to be an active and recyclable catalyst in the aerobic oxidation of alcohols and amines by atmospheric oxygen.

Ionothermal synthesis was unveiled around 10 years ago, but its unexpected suitability for preparing porous materials is a young topic, full of promise. We believe that the present findings can be extended to a larger number of polymerization systems by careful selection of molten salts (including ionic liquids), opening up a new and sustainable pathway to porous materials (Supplement Note 1).

Notes and references

^a Chemical Science Division, Oak Ridge National Laboratory, Oak Ridge 37831, Tennessee, USA. E-mail: chemistryzpf@163.com; dais@ornl.gov

^b Department of Chemistry, University of Tennessee, Knoxville 37996, Tennessee, USA.

† Electronic Supplementary Information (ESI) available: Supplementary Figures, Tables and Notes. See DOI: 10.1039/b000000x/

- Y. Zhu, S. Murali, M. Stoller, K. J. Ganesh, W. Cai, P. J. Ferreira, A. A. Pirkle, R. M. Wallace, K. A. Cychoz, M. Thommes, D. Su, E. A. Stach and R. S. Ruoff, *Science*, 2011, **332**, 1537–1541.
- A. K. Geim and K. S. Novoselov, *Nat. Mater.*, 2007, **6**, 183–191.
- K. S. Kim, Y. Zhao, H. Jang, S. Y. Lee, J. M. Kim, K. S. Kim, J. H. Ahn, P. Kim, J. Y. Choi and B. H. Hong, *Nature*, 2009, **457**, 706–710.
- M. Choucair, P. Thordarson and J. A. Stride, *Nat. Nanotechnol.*, 2009, **4**, 30–33.
- Z. Sun, Z. Yan, J. Yao, E. Beitler, Y. Zhu and J. M. Tour, *Nature*, 2010, **468**, 549–552.
- Y. Liang, Y. Li, H. Wang, J. Zhou, J. Wang, T. Regier and H. J. Dai, *Nat. Mater.*, 2011, **10**, 780–786.
- M. J. Allen, V. C. Tung and R. B. Kaner, *Chem. Rev.*, 2010, **110**, 132–145.
- S. Park and R. S. Ruoff, *Nat. Nanotechnol.*, 2009, **4**, 217–224.
- J. M. Cai, P. Ruffieux, R. Jaafar, M. Bieri, T. Braun, S. Blankenburg, M. Muoth, A. P. Seitsonen, M. Saleh, X. L. Feng, K. Müllen and R. Fasel, *Nature*, 2010, **466**, 470–473.
- S. J. Guo, and S. J. Dong, *Chem. Soc. Rev.*, 2011, **40**, 2644–2672.
- X. H. Li, S. Kurasch, U. Kaiser and M. Antonietti, *Angew. Chem. Int. Ed.*, 2012, **51**, 9689–9692.
- X. H. Li and M. Antonietti, *Angew. Chem. Int. Ed.*, 2013, **52**, 4572–4576.
- X. Liu and M. Antonietti, *Adv. Mater.*, 2013, **25**, 6284–6290.
- X. Liu, C. Giordano and M. Antonietti, *Small*, 2014, **10**, 193–200.
- C. N. R. Rao, A. K. Sood, K. S. Subrahmanyam, A. Govindaraj, *Angew. Chem. Int. Ed.*, 2009, **48**, 7752–7777.
- Y. Fang, Y. Lv, R. Che, H. Wu, X. Zhang, D. Gu, G. Zheng and D. Y. Zhao, *J. Am. Chem. Soc.*, 2013, **135**, 1524–1530.
- G. P. Mane, S. N. Talapaneni, C. Anand, S. Varghese, H. Iwai, Q. Ji, K. Ariga, T. Mori and A. Vinu, *Adv. Funct. Mater.*, 2012, **22**, 3596–3604.
- J. Liu, T. Yang, D. Wang, G. Q. Lu, D. Y. Zhao and S. Z. Qiao, *Nature Commun.*, 2013, **4**, 2798.
- J. Lee, J. Kim and T. Hyeon, *Adv. Mater.*, 2006, **18**, 2073–2094.
- S. Jun, S. H. Joo, R. Ryoo, M. Kruk, M. Jaroniec, Z. Liu, T. Ohsuna and O. Terasaki, *J. Am. Chem. Soc.*, 2000, **122**, 10712–10713.
- D. Pech, M. Brunet, H. Durou, P. Huang, V. Mochalin, Y. Gogotsi, P. Taberna and P. Simon, *Nat. Nanotechnol.*, 2010, **5**, 651–654.
- M. R. Lukatskaya, O. Mashtalir, C. E. Ren, Y. Dall’Agnese, P. Rozier, P. L. Taberna, M. Naguib, P. Simon, M. W. Barsoum and Y. Gogotsi, *Science*, 2013, DOI: 10.1126/science.1241488.
- W. G. Pell, B. E. Conway and N. Marincic, *J. Electroanal. Chem.*, 2000, **491**, 9–21.
- L. Wang, T. Masahiro and I. Michio, *New Carbon Mater.*, 2008, **23**, 111–115.
- X. Liu, N. Fechner and M. Antonietti, *Chem. Soc. Rev.*, 2013, **42**, 8237–8265.
- L. Y. Zhao, R. He, K. T. Rim, T. Schiros, K. S. Kim, H. Zhou, C. Gutiérrez, S. P. Chockalingam, C. J. Arguello, L. Pálová, D. Nordlund, M. S. Hybertsen, D. R. Reichman, T. F. Heinz, P. Kim, A. Pinczuk, G. W. Flynn and A. N. Pasupathy, *Science*, 2011, **333**, 999–1003.
- K. Gong, F. Du, Z. Xia, M. Durstock and L. M. Dai, *Science*, 2009, **323**, 760–764.
- P. F. Zhang, J. Yuan, T. Fellingner, M. Antonietti, H. Li and Y. Wang, *Angew. Chem. Int. Ed.*, 2013, **52**, 6028–6032.
- P. F. Zhang, Y. Gong, H. R. Li, Z. R. Chen and Y. Wang, *Nature Commun.*, 2013, **4**, 1593.
- B. S. Ghanem, N. B. McKeown, P. M. Budd, N. M. Al-Harbi, D. Fritsch, K. Heinrich, L. Starannikova, A. Tokarev and Y. Yampolskii, *Macromolecules*, 2009, **42**, 7881–7888.
- X. Li, W. Xing, S. Zhuo, J. Zhou, F. Li, S. Z. Qiao and G. Q. Lu, *Bioresour. Technol.*, 2011, **102**, 1118–1123.
- A. Elmouwahidi, Z. Zapata-Benabithé, F. Carrasco-Marín and C. Moreno-Castilla, *Bioresour. Technol.*, 2012, **111**, 185–190.
- C. Peng, X. Yan, R. Wang, J. Lang, Y. Ou and Q. Xue, *Electrochim. Acta*, 2013, **87**, 401–408.
- J. Zhu, K. Kailasam, A. Fischer and A. Thomas, *ACS Catal.*, 2011, **1**, 342–347.
- B. Li, H. Cao, J. Shao, G. Li, M. Qu and G. Yin, *Inorg. Chem.*, 2011, **50**, 1628–1632.
- H. Kim, D. Seo, S. Kim, and K. Kang, *Carbon*, 2011, **49**, 326–332.